Bioorganic Chemistry 92 (2019) 103282

Contents lists available at ScienceDirect

Bioorganic Chemistry

journal homepage: www.elsevier.com/locate/bioorg

Rational design of some substituted phenyl azanediyl (bis) methylene phosphonic acid derivatives as potential anticancer agents and imaging probes: Computational inputs, chemical synthesis, radiolabeling, biodistribution and gamma scintigraphy

Mohammed A. Khedr[a], Hassan M. Rashed[b,c,*], Hamed Farag[d], Tamer M. Sakr[e,*]

[a] Pharmaceutical Chemistry Department, Faculty of Pharmacy, Helwan University, Postal Code: 11795, Cairo, Egypt
[b] Labeled Compounds Department, Hot Labs Center, Atomic Energy Authority, P.O. Box 13759, Cairo, Egypt
[c] Department of Pharmaceutics, Faculty of Pharmacy, Sinai University, Egypt
[d] Radiotherapy and Nuclear Medicine Department, National Cancer Institute, Cairo University, Cairo, Egypt
[e] Radioactive Isotopes and Generator Department, Hot Labs Center, Atomic Energy Authority, P.O. Box 13759, Cairo, Egypt

ARTICLE INFO

Keywords:
Rational design
Bis (methylene phosphonic acid)
Docking
Molecular dynamics
Radiolabeling/Gamma scintigraphy

ABSTRACT

Bisphosphonates are widely used for treatment of osteoporosis. Recently, they have been reported to be effective anticancer agents. In this work, we designed some substituted phenyl (azanediyl) bis (methylene phosphonic acid) to be tested for their anticancer effect. Both molecular docking and dynamics studies were used to select the top ranked highly scored compounds. The selected hits showed potential *in vitro* anticancer effect against some cell lines. Biodistribution pattern and gamma scintigraphy were conducted to the most effective derivative **(BMBP)** after radiolabeling with ^{99m}Tc. Results of biodistribution and scintigraphic imaging of **^{99m}Tc-BMBP** in tumor bearing mice showed a notable tumor affinity, and confirmed the targeting affinity of **BMBP** to the tumor tissues. As a conclusion, BMBP could act as potential anticancer agent and imaging probe.

1. Introduction

Bone-seekers (compounds that have a high affinity to bones) are used in complexes with radioisotopes as imaging agents for bone tumors [1–3]. Their uptake into bone is still under investigation to understand the real mechanism, but the main uptake mechanism can be attributed to their coordination features with metals especially calcium [3–5]. Technetium-99 m is one of the most used radioisotopes in complex with bone seekers due to its excellent diagnostic characteristics ($t_{1/2}$ of 6 h and gamma energy = 140 KeV) [6,7]. The bone-seekers needs specific ligands to complex with in order to direct the complex to the binding sites of bone tissue [3].

Bisphosphonates (BPs) are a class of drugs, with high affinity for bone tissues, that can form a complex with bone seekers easily [8,9]. Examples of BPs are etidronate, clodronate, pamidronate, alendronate, risedronate, ibandronate and zoledronate [10,11]. BPs' mode of action is *via* inhibition of human farnesyl pyrophosphate synthase (HFPPS) that is found in bone tissue that can be considered the main target of their action. ^{99m}Tc-methylene diphosphonate (^{99m}Tc-MDP) and ^{99m}Tc-ethanediyl bis [nitrilo bis-(methylene)] tetrakis-phosphonic acid (^{99m}Tc-EDTMP) are examples of ^{99m}Tc-BP complexes used for bone imaging [12,13]. The presence of anionic phosphonate groups results in chelation of calcium ions; besides attaining strong binding with the HFPPS binding sites that features cationic properties [14–16]. The HFPPS inhibitors have been reported to have anticancer activity [17,18].

In our previous study, we have reported that a one carbon linker between the –N atom and the phosphonate group may be useful for getting better fitting and high affinity toward farnesyl pyrrophosphatase synthase enzyme [2]. The study was for a natural compound. The main aim of this study was to maximize the pharmacodynamic interactions of BPs *via* optimization of the chemical structure by some modifications that aimed to increase its affinity of binding to farnesyl pyrrophosphatase synthase enzyme, then, choosing the best compounds with high affinity to be tested and evaluated for their anticancer effect. Tracking the biodistribution using radiolabeling technique was the best choice for assessment of the selectivity of our compounds toward tumor cells.

* Corresponding authors at: Hot Labs Center, Atomic Energy Authority, P.O. Box 13759, Cairo, Egypt (H.M. Rashed & T.M. Sakr).
E-mail addresses: Hassan_vodafone@hotmail.com (H.M. Rashed), Tamer_sakr78@yahoo.com, Tmmhafez@msa.eun.eg (T.M. Sakr).

https://doi.org/10.1016/j.bioorg.2019.103282
Received 15 June 2019; Received in revised form 10 September 2019; Accepted 11 September 2019
Available online 12 September 2019
0045-2068/

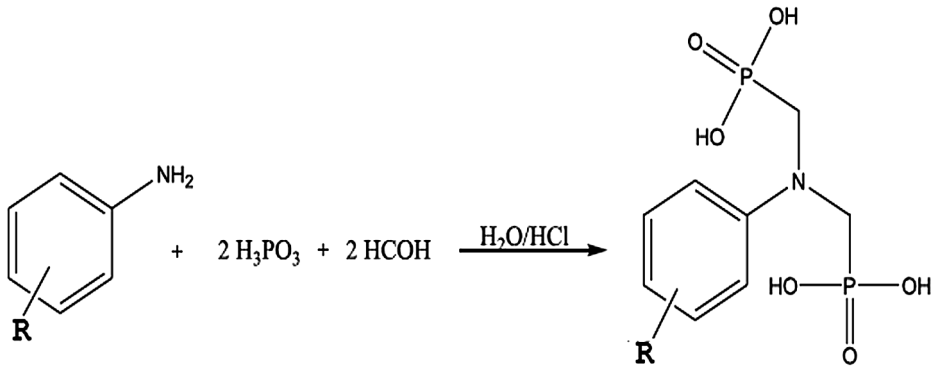

R = 4-Cl, 4-F, 4-Br, 2-Br-5-CH3, 4-CF3

Scheme 1. The synthetic pathway for the proposed compounds.

2. Experimental

2.1. Materials

All chemicals were purchased from Sigma-Aldrich. Chemical synthesis was conducted as per scheme 1 synthesis pathway. The used mice weight was in the range of (20–25 g). All mice were males and from the type Swiss albino. They were supplied from the National Cancer Institute (Doki, Egypt). Molecular Operating Environment MOE 2016.08 was purchased from Chemical Computing Group Inc. (Montreal, QC, Canada). HPLC is Hitachi model, Alpha bond RP-18 C18 125A 10U column with I.D. 3.9 and length 300 mm, with UV spectrophotometer detector (SPD-6A), and consists of pumps LC-9A, Japan. Chemical reactions were monitored using analytical thin layer chromatography (TLC) with Merck 60F-254 silica-gel plates. Melting Point apparatus was used to check the melting points. Nuclear magnetic resonance (NMR) spectra were performed by using dimethyl sulphoxide (DMSO)-d_6 solvent and tetramethyl silane (TMS) as internal standard with 400 MHz Bruker spectrometer. Chemical shifts were showed in ppm downfield from TMS and splitting pattern is abbreviated as s, singlet; m, multiplet and d, doublet. Infrared spectra were recorded using Shimadzu FTIR infrared spectrophotometer. Mass spectroscopy was performed using Accela 1200 LC-10AD pump.

2.2. Molecular docking

2.2.1. Molecular docking using MOE 2016.08

The 3D structure of HFPPS was obtained from pdb (code = 2f92) with resolution of 2.15 Å. Alendronate was the ligand that is co-crystallized with the protein. All coordinates were derived from pdb. The used docking protocol was the triangle matcher as a placement method. London dG and MMFF94x were used as a rescoring method and Force field, respectively.

2.2.2. Molecular dynamics simulations

The simulations were performed using MOE package. The ideal pose of top ranked hits was kept inside the active site. The hydrogen atoms were added then the energy was minimized. Any solvent molecules in the system were deleted before the solvation followed by the addition of the salt atoms to the system in a spherical shape. Force field was selected as Amber 10:EHT. All non-boned interactions were enabled. The temperature was increased from 0 to 300 K. Then this step was followed by equilibration and cooling until to 0 K was reached. The simulation was conducted over 30 ns period of time.

2.3. Chemical synthesis

2.3.1. General method for the synthesis of azanediyl (bis) methylene phosphonic acid derivatives

The compounds were synthesized according to Irani-Moedritzer method [19]. A mixture of phosphorous acid (0.1 mol) and aromatic amines (0.2 mol) in 100 ml ethanol and 50 ml of HCL was prepared. The mixture was refluxed for 3 h at 110 °C. Paraformaldehyde (0.4 mol) was added portion wise to the mixture. The reaction was kept at 110 °C for an additional three hours with stirring, in parallel; the reaction was monitored using TLC. At the end of the reaction, solvent was evaporated by a rotaevaporator and the crude product was obtained. The pure product was received by recrystallization in ethanol (Scheme 1).

2.3.1.1. 4-Chloro phenyl azanediyl (bis) methylene phosphonic acid II. Brown solid; yield 71%; M.P. 164–166 °C, ^{1}HNMR δ ppm: δ 1.96 (s, 4H, CH_2), δ 4.5 (s, 1H, P(O)−$(OH)_2$), δ 7.2 (d, 2H, J = 8.3 Hz), δ 7.51 (d, 2H, J = 8.3 Hz). IR; P═O stretching at (1140–1210) cm^{-1}, P−O stretching (730–800) cm^{-1}, P−C stretch (650–700), 4 (OH) at 3695. 3670, 3660, 3645 cm^{-1}. C═C aromatic (1550–1660) cm^{-1}. MS *m/z* %: 313 (63%), 315 (21%), 234 (100%), 219 (6.8%), 186 (51.8%), 140 (30.3%), 128 (12.8%), 110 (47%), 112 (65%), 94.9 (92.9%) and 80.9 (71.4%).

2.3.1.2. 4-Fluoro phenyl azanediyl (bis) methylene phosphonic acid III. Yellowish brown solid; yield 82%; M.P. 158–160 °C, ^{1}HNMR δ ppm: δ 1.89 (s, 4H, CH_2), δ 4.7 (s, 1H, P(O)−$(OH)_2$), δ 7.3 (d, 2H, J = 8.3 Hz), δ 7.7 (d, 2H, J = 8.3 Hz). IR; P−C stretch (650–700), P═O stretching at (1140–1210) cm^{-1}, P−O stretching (730–800) cm^{-1}, P−C stretch (650–700), 4 (OH) at 3685. 3681, 3667, 3655 cm^{-1}.C═C aromatic (1555–1668) cm^{-1}. MS *m/z* %: 297 (35%), 282 (12.5%), 220 (8%), 218 (65.6%), 186 (100%), 203.9 (1.5%), 124 (30.3%), 94.9 (92%) and 80.9 (70%).

2.3.1.3. 4-Bromo phenyl azanediyl (bis) methylene phosphonic acid V. Dark brown solid; yield 77%; M.P. 179–181 °C, ^{1}HNMR δ ppm: δ 1.92 (s, 4H, CH_2), δ 4.2 (s, 1H, P(O)−$(OH)_2$), δ 7.5 (d, 2H, J = 8.3 Hz), δ 7.7 (d, 2H, J = 8.3 Hz). IR; P−C stretch (650–700), P═O stretching at (1140–1210) cm^{-1}, P−O stretching (730–800) cm^{-1}, P−C stretch (650–700), 4 (OH) at 3688. 3675, 3662, 3645 cm^{-1}.C═C aromatic (1550–1660) cm^{-1}. MS *m/z* %: 358.9 (49.8%), 360.9 (50%), 341 (12.6%), 279.9 (8.1%), 277 (100%), 183 (30.3%), 186 (51.8%), 155 (65.4%), 94.9 (90%) and 80.9 (70.5%).

2.3.1.4. 2-Bromo-5-methyl phenyl azanediyl (bis) methylene phosphonic acid VI. Brown crystals; yield 74%; M.P. 148–150 °C, ^{1}HNMR δ ppm: δ

1.98 (s, 4H, CH_2), δ 4.6 (s, 1HP(O)−$(OH)_2$), δ 7.6 (d,d 2H), δ 6.5 (s, 1H), δ 2.5 (s, 3H). IR; P−C stretch (650–700), P=O stretching at (1140–1210) cm^{-1}, P−O stretching (730–800) cm^{-1}, P−C stretch (650–700), 4 (OH) at 3690. 3674, 3661, 3657 cm^{-1}. C=C aromatic (1553–1667) cm^{-1}. MS *m/z* %: 372 (40%), 374 (41%), 291 (66.1%), 277 (6.4%), 197 (30.6%), 168 (100%), 94 (96%) and 80 (70.3%).

2.3.1.5. 4-(Trifluoromethyl) phenyl azanediyl (bis) methylene phosphonic acid VII. Yellow solid; yield 84%; M.P. 188–190 °C, ^{1}HNMR δ ppm: δ 1.93 (s, 4H, CH_2), δ 4.8 (s, 1H, P(O)−$(OH)_2$), δ 7.6 (d, 2H, J = 8.3 Hz), δ 7.8 (d, 2H, J = 8.3 Hz). IR; P−C stretch (650–700), P=O stretching at (1140–1210) cm^{-1}, P−O stretching (730–800) cm^{-1}, P−C stretch (650–700), 4 (OH) at 3680. 3677, 3670, 3660 cm^{-1}.C=C aromatic (1550–1665) cm^{-1}. MS *m/z* %: 349 (13%), 330 (12%), 280 (8.3%), 254 (16%), 236 (100%), 203 (11.7%), 186 (45.7%), 174 (16%), 146 (34.4%), 127 (17.2%), 110 (26.3%) and 80 (73%).

2.4. In vitro evaluation of HFPPS enzyme inhibition

Cell line derived from human lung carcinoma A549 was purchased from the American Type Culture Collection. The cell line was cultured in Dulbecco's modified Eagle's medium with 10% fetal bovine serum and incubated at 37 °C in a humidified atmosphere containing 5% CO_2 in air.

The concentrations of 10, 25, 50 and 100 μg/ml for the compounds were added to tissue culture dishes, and then cells were incubated for 24 h. The cells were allowed to grow for 48 h and then processed for analyses. Control group was used and triplicate cultures were set up for each concentration and for control. Each step was repeated three times. Sample protein content was determined using Bradford method [20].

HFPPS activity was evaluated in A549 cells treated with the tested compounds at 10 μg/ml, 25 μg/ml, 50 μg/ml and 100 μg/ml for 48 h. In ELISA, the wells were pre-coated with HFPPS monoclonal antibody. After incubation, a biotin-conjugated anti HFPPS antibody was added for allowing it to bind to HFPPS. After incubation unbound biotin-conjugated was decanted. Anti-HFPPS antibody was washed away. Streptavidin-HRP was added to the biotin- conjugated Anti-HFPPS antibody. Substrate solution was added and color developed in proportion to the amount of HFPPS. The absorbance was measured at 450 nm [21].

2.5. Statistical analysis

The mean ± SEM was calculated, (ANOVA) analysis followed by Turkey-Kramer test for multiple comparisons were done. Graph Pad Instant (version 3.05) was used for the statistical software.

2.6. Radiolabeling of compound BMBP

2.6.1. ^{99m}Tc-BMBP complex preparation

Radiolabeling of **BMBP** by ^{99m}Tc was achieved by using the direct labeling method by sodium dithionite ($Na_2S_2O_4$) [22–24]. The process of labeling can be affected by; **BMBP** amount, $Na_2S_2O_4$ amount, pH, reaction time and temperature. All these factors were investigated [25–27]. Each experiment was performed in triple and one-way ANOVA test was used to evaluate data differences (level of significance set at $P < 0.05$).

To 750 μL of **BMBP** solution in DMSO containing (0.2–2 mg) of **BMBP**, 500 μL of freshly prepared $Na_2S_2O_4$ was added. Then, 200 μL of $^{99m}TcO_4^-$ (51.5 MBq) eluted from ^{99}Mo/^{99m}Tc generator were added dropwise to reaction vial. The pH was adjusted by 0.05 M sodium hydroxide and/or 0.05 M HCl solutions. The reaction was monitored at different temperatures during different time intervals (5–60 min).

2.6.2. Analysis of the radiochemical yield

The radiochemical yield of radiolabeling process and stability of **^{99m}Tc-BMBP** complex *in-vitro* were evaluated by ascending paper chromatography (P.C.) and TLC to determine the percent of **^{99m}Tc-BMBP**, free $^{99m}TcO_4^-$ and colloidal $^{99m}TcO_2$ [28,29]. Acetone (as a mobile phase) was used to determine the free $^{99m}TcO_4^-$ percentage (R_f = 1) and 0.5 N NaOH was used to determine the colloidal $^{99m}TcO_2$ percentage (R_f = 0) [24,30–32].

The radiochemical purity was further confirmed by a HPLC. The HPLC analysis of **^{99m}Tc-BMBP** complex was done by injection of 10 μL **^{99m}Tc-BMBP** complex, after 0.22 μm Millipore filtration, into the RP-18 column and UV spectrophotometeric detector was operated at a 282 nm.

2.6.3. in-vitro stability of ^{99m}Tc-BMBP complex

The reaction was left at ambient room temperature for 24 h then different samples at different time periods were collected and tested for their radiochemical yields [32].

2.7. Pharmacokinetic study of ^{99m}Tc-BMBP complex

2.7.1. Induction of tumor in mice

Ehrlich ascites carcinoma was used to induce solid tumor in mice [25,33,34]. The tumor was derived from a donor female Swiss albino mouse (7 days old) and diluted with sterile physiological saline solution. Carefully, 0.2 ml of the previous solution were injected in the right thigh muscle of male Albino mice. After 7 to 10 d, a palpable solid tumor with a volume ranged 0.9 ± 0.1 cm^3 was observed and used for the biological studies [34–37].

2.7.2. Biodistribution of the ^{99m}Tc-BMBP complex in tumor model

This study was approved by the animal ethics committee of Egyptian Atomic Energy Authority. Mice, with weight 20–25 g, were segregated in groups of five and fed up with food and water. Aliquots of 150 μL containing 5.2 MBq of **^{99m}Tc-BMBP** complex were injected intravenously in male Swiss albino mice with palpable solid tumor in right thigh muscle. Mice were anaesthetized and dissected at 0.5, 1, 2, 3 and 4 h post-injection. Each mouse was weighed and fresh blood, bone and muscle samples were separated, weighed and their radioactivities were counted. Blood, bone and muscles were calculated in percentage of 7, 10 and 40% of the total body weight, respectively [35,38]. Other organs and tissues were also collected, weighed and their radioactivities were counted using NaI (Tl) crystal gamma counter. Percent-injected dose per organ (% ID/organ ± S.D.) at each time point for a population of five mice were reported. One-way ANOVA test was used to evaluate data differences ($P < 0.05$).

2.8. Gamma scintigraphy of ^{99m}Tc-BMBP complex

The scintigraphic imaging of mice was performed using a dual-head variable angle γ-camera.**^{99m}Tc-BMBP** biodistribution in mice (with solid tumor in right thigh muscle) was recorded in the gamma camera with a pinhole collimator of 5-mm, window setting of 140 KeV and width of 20%. Approximately 0.15 ml of **^{99m}Tc-BMBP** solution containing 141 μCi was IV injected in solid tumor bearing mice. Before injection, the administered radioactive dose to each mouse was measured by an ionization chamber detector. Each mouse was anesthetized by intraperitoneal injection of thiopental (5 mg/kg) before imaging. Images were taken at 10 min scintigraphy scan at different time intervals (1, 2 and 4 h post injection). The images were saved in a 512 × 512 matrix size with 300 s acquisition time [39–41].

3. Results and discussion

The amino alkyl phosphonic acid moiety was reported in some nitrogenous bisphosphonates (Fig. 1). The amino phosphonic acids are biologically active compounds and highly reactive toward coordination with metal ions [19].

To date, the α-amino alkyl phosphonic acid derivatives have not

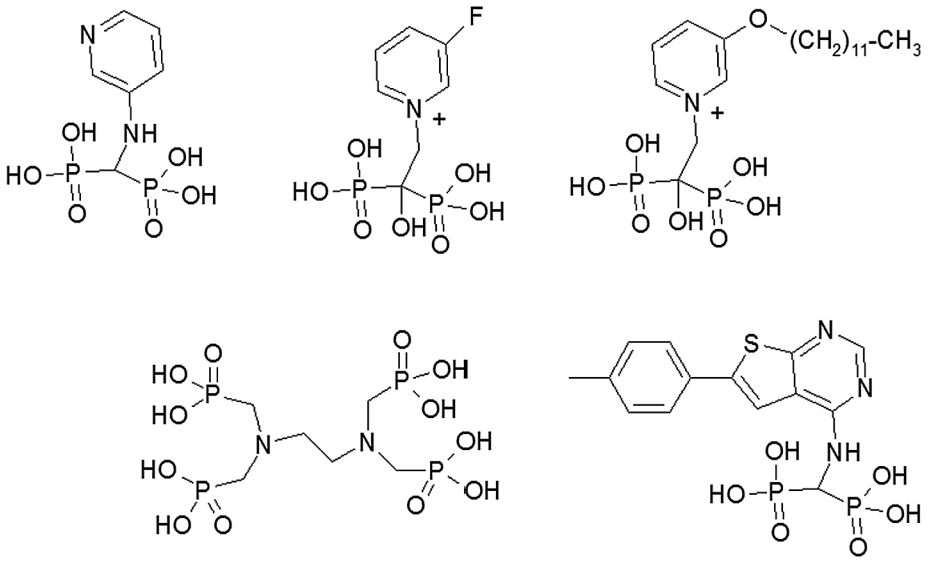

Fig. 1. Chemical structure of some reported biologically active amino phosphonic acid derivatives.

been isolated from living organisms nor from natural source. Some derivatives were synthesized chemically; however, the phosphonate groups were in a germinal configuration. The azanediyl (bis) methylene phosphonic acid scaffold and its inhibitory activity against HFPPS enzyme were not reported as well. In our previous work we reported that; one carbon linker between the amino and the phosphonic group can result in a potential compounds with high affinity to HFPPS. To date, the substituted phenyl amino methylene phosphonic acid derivatives have not been reported for their inhibitory activity against HFPPS enzyme. Some designed compounds with azanediyl (bis) methylene phosphonic acid scaffold were docked against HFPPS to select the top ranked compounds with the best scores in both in silico affinity and free energy of binding. The structure of the top-scored **Compound VI (BMBP)** was then evaluated by a molecular dynamic study to test its binding stability. In addition, the docking of this compound in complex with ^{99m}Tc was done before conduction of the biodistribution experiment. The top selected compounds were evaluated biologically.

3.1. Molecular docking study

The molecular docking study of the proposed structure VI with 4-(2-Br-5-CH3) phenyl substitution had showed the best **ΔG** with both MOE (−18.07 kcal/mol) and Leadit (−26.75 kcal/mol). As a result, its affinity was the top ranked (51.11) among the tested compounds (Table 1). The analysis of the docking revealed that proposed **compound VI** showed two salt bridges with both Lys257, and Arg112. In addition to a number of strong hydrogen bonding with Asp243, Asp103, Asp 107 and coordination with Zn ++ ions found in the active site of HFPPS (Fig. 2**E**).

Compounds II, III, V, VI, and VIII showed the highest docking scores among all proposed compounds. Both compounds III and V showed interactions with Asp103, Asp107, and Arg112 (Fig. 2**D and B**), respectively. Compound VII showed one salt bridge with Arg112 and some hydrogen bonds with Asp174, Asp243, and Asp103.

Compound III with 4-fluoro substitution and compound VII with 4-trifluoromethyl substitution shared the same binding mode in which coordination with two ZN++ in addition to two salt bridges with Lys257 and Arg112 (Fig. 2**C and D**).

The top ranked **Compound VI (BMBP)** with 2-bromo-5-methyl substitution was selected for molecular dynamic study to evaluate its stability of binding because it showed the highest affinity value 51.11 and the best docking score as well.

The proposed VI-TC complex was docked as well (Fig. 2**F**) and showed a network of coordination with three ZN++ and a number of hydrogen bonds with Asp174, Asp261. Two salt bridges with Lys257 and Arg112 were also retained.

Table 1
Molecular docking results of the proposed compounds using both Leadit and MOE programs.

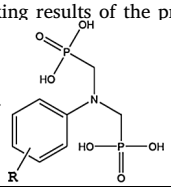

Proposed compound	R group	Leadit ΔG (kcal/mol)	Affinity pki	ΔG (MOE2016.08) (kcal/mol)
I	H	−21.84	31.95	−12.75
II	4-Cl	−23.65	34.71	−15.47
III	4-F	−24.40	34.46	−15.21
IV	3-F	−24.33	33.04	−15.25
V	4-Br	−25.74	35.42	−15.87
VI	2-Br-5-CH_3	−26.75	51.11	−18.07
VII	4-CF_3	−25.50	34.68	−16.28
VIII	4-CH_3	−18.55.	20.47	−13.02
IX	4-$(CH3)_2$-N	−16.78	20.34	−12.58
X	4-OH	−15.67	19.77	−14.26

3.2. Molecular dynamics

In order to validate the binding mode and docking results, molecular dynamics (MD) simulations were carried out for the top ranked **Compound VI (BMBP)**. Throughout the simulation period, no significant fluctuations were observed in the backbone of the protein. To ensure the binding stability of **Compound VI (BMBP)** in the active site, ligand positional RMSD was analyzed (Fig. 3). The RMSD started at 0.9 Å with some fluctuations until reached the equilibrium at 1.4 Å after 10 ns period of time.

3.3. Synthesis of the proposed compounds

The synthesis of methylene phosphonic acids derivatives was achieved by Mannich-type reaction. The substituted aromatic primary amines were allowed to react with phosphorous acid and formaldehyde in presence of hydrochloric acid. The hydrogen atom attached to the phosphorous atom in phosphorous acid is considered acidic hydrogen

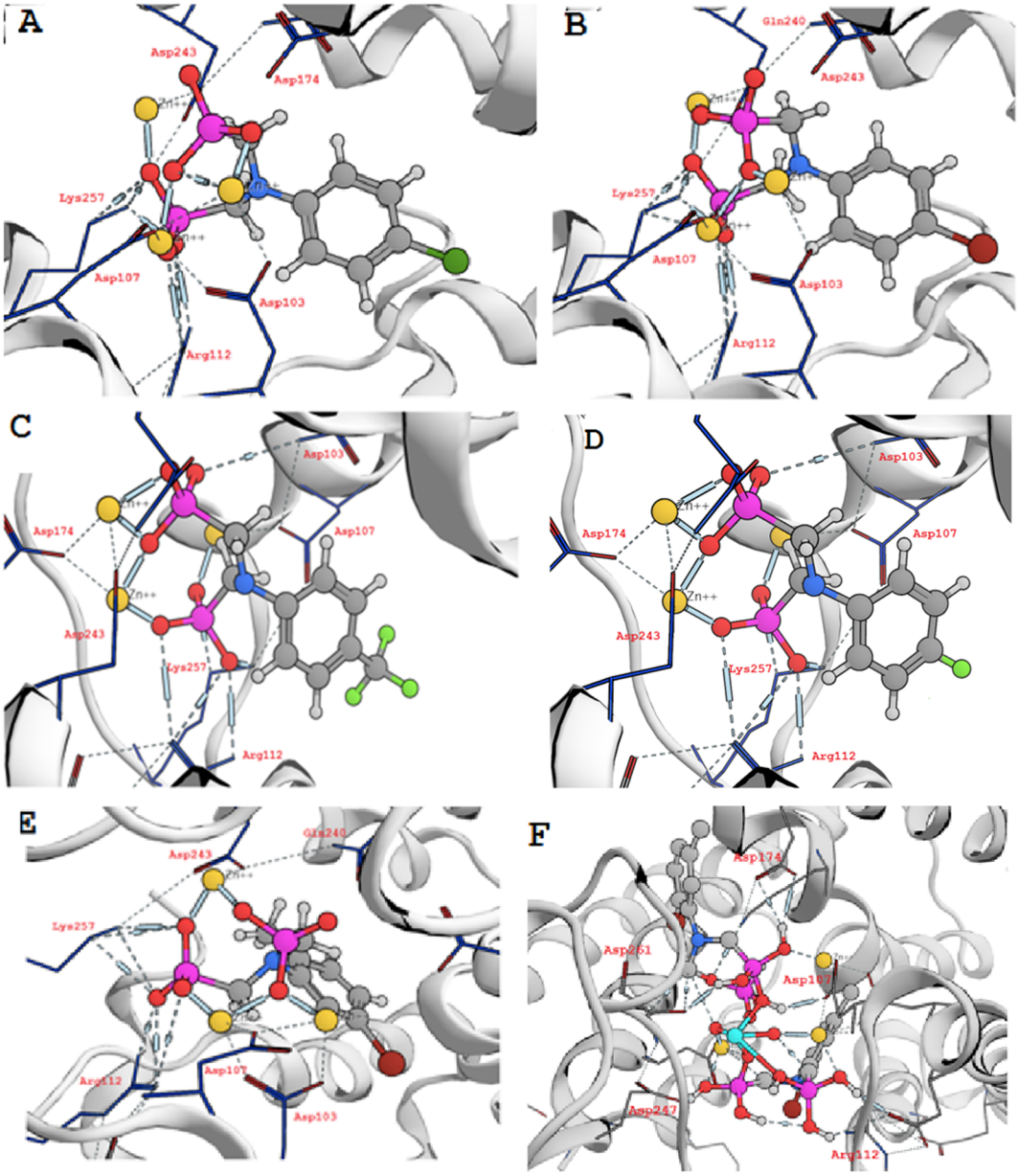

Fig. 2. The best docking pose for (A) compound II, (B) compound V, (C) compound VII, (D) compound III, (E) compound VI and (F) compound VI in complex with ^{99m}Tc.

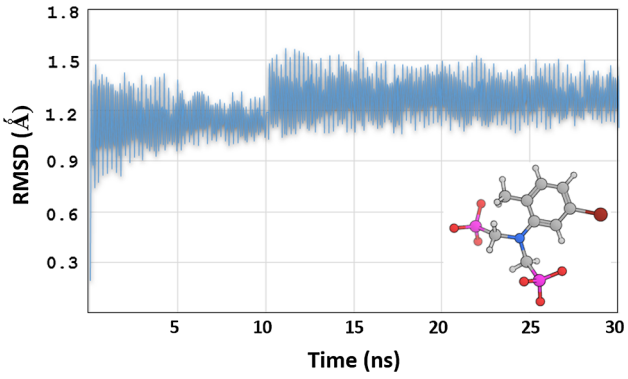

Fig. 3. Molecular dynamic simulations for compound VI during 30 ns.

that will be replaced to facilitate the reaction. The chemical structures of the obtained compounds were characterized by ^{1}HNMR, IR and MS spectroscopic data. The IR spectra confirmed the P—C stretch (650–700), P═O stretching at (1140–1210) cm^{-1}, P—O stretching (730–800) cm^{-1}, and P—C stretch (650–700) peaks. The presence of methylene group $-CH_2$ attached to the phosphonate group was also confirmed. All synthesized compounds showed common peaks at MS spectra for the cleaved protonated phosphonate group at MS *m/z* %: 80.9 (70–71%) and (CH_2 = P(O)—$(OH)_2$) at MS *m/z* %:94.9 (90–96%).

3.4. Biological results HFPPS

In order to provide an evidence that the newly designed and synthesized bisphosphonate analogues have an inhibitory activity against HFPPS enzyme, an *in vitro* ELISA assay was performed. According to the

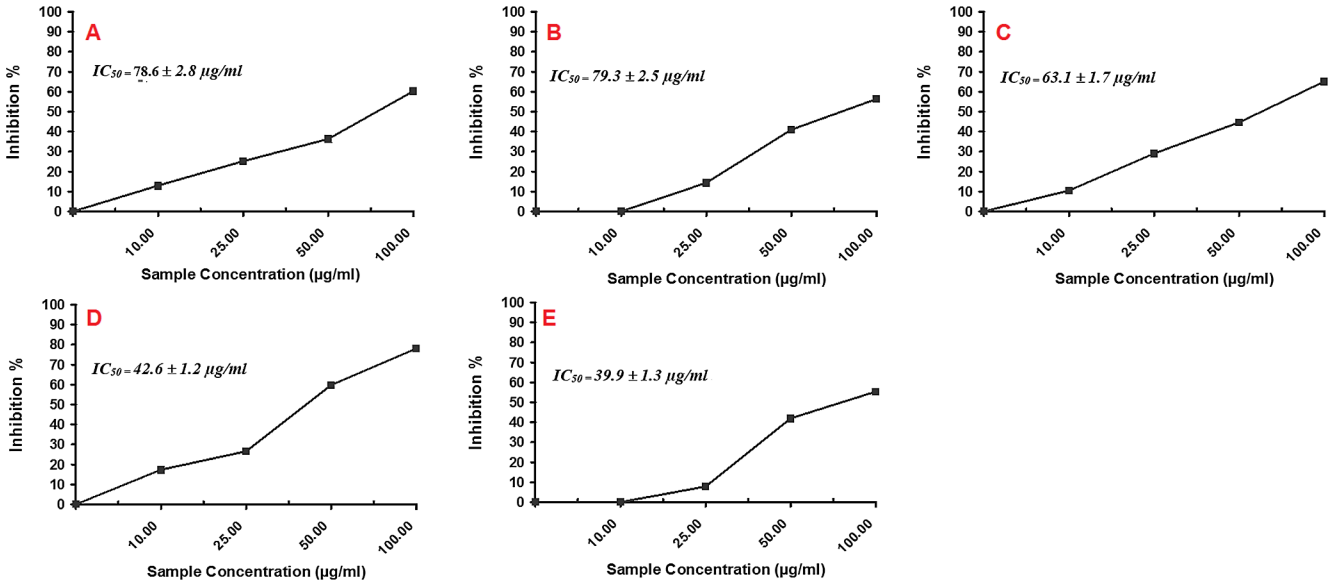

Fig. 4. The inhibitory activity against HFPPS enzyme.

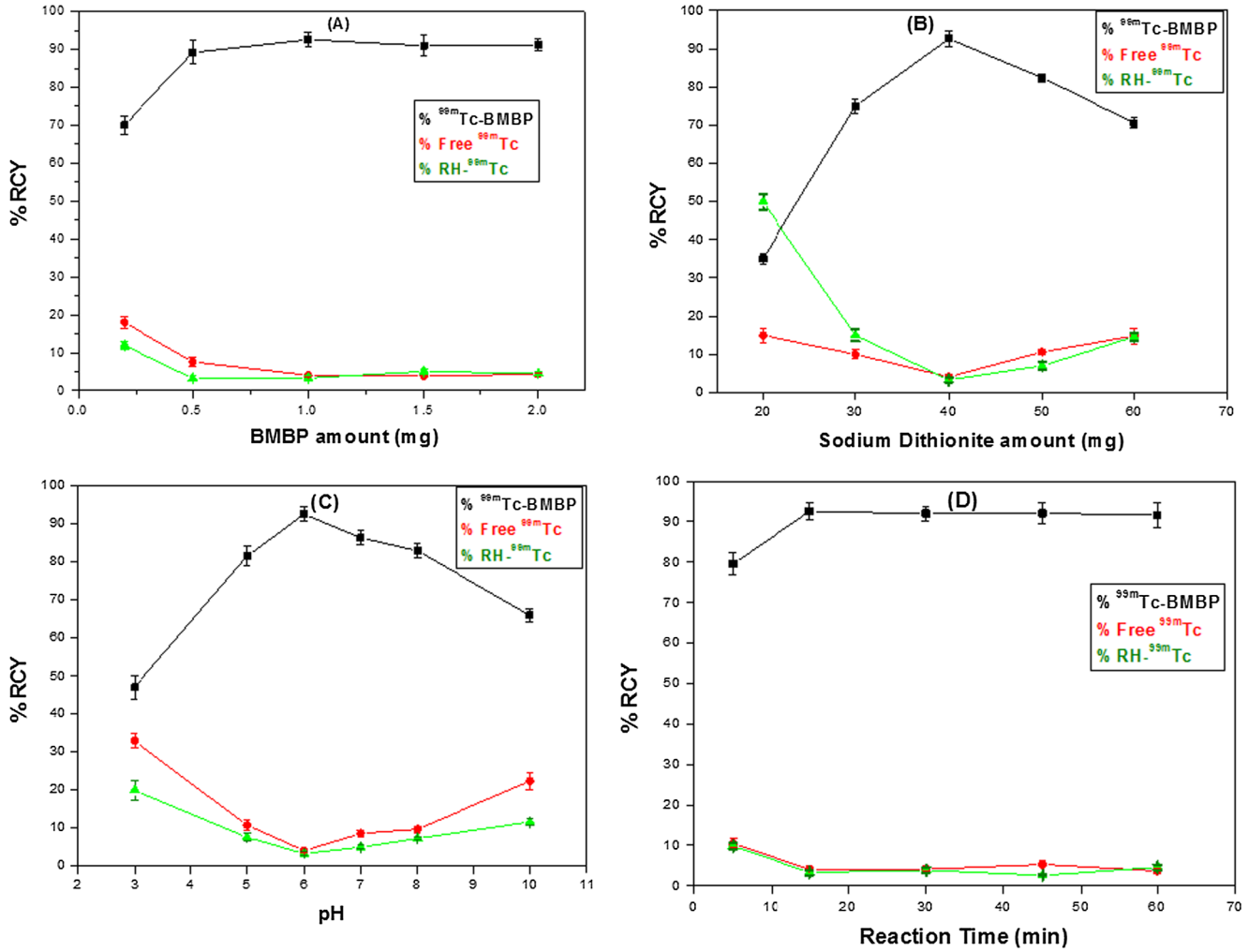

Fig. 5. Percentage of the radiochemical yield obtained at different BMBP amounts (A), $Na_2S_2O_4$ amounts (B), pH values (C) and reaction times (D).

results, **Compound VI (BMBP)** achieved the best inhibitory activity with IC_{50} of 39.9 µg/ml. Compound V showed IC_{50} of 42.6 µg/ml. While compound VII showed IC_{50} of 63.1 µg/ml. Compounds II and III showed close results of 78.6 and 79.3 µg/ml respectively (Fig. 4). **Compound VI (BMBP)** and compound V confirmed their ability to inhibit HFPPS which confirmed the computational results. They may need further

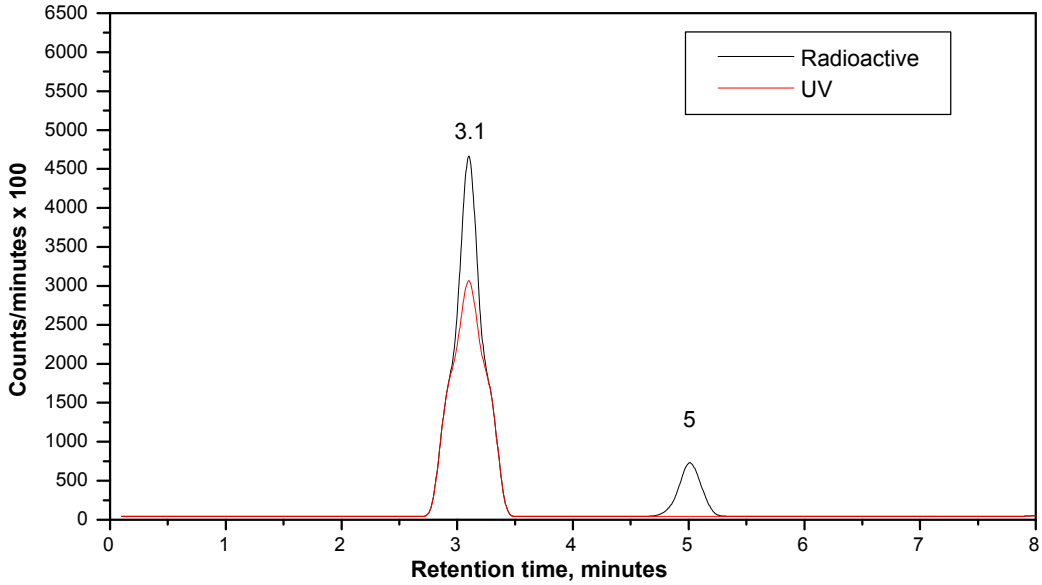

Fig. 6. Overlaid chromatograms of BMBP and ^{99m}Tc-BMBP.

study and optimization in the future.

3.5. Radiolabeling of compound BMBP

From the above sections, it was very clear that **compound VI (BMBP)** is the most superior synthesized compound in its *in-vitro* efficacy, so the next step was evaluation of its *in-vivo* tumor targeting. To attain this, radiolabeling approach was conducted to be able to trace that compound inside the animal organs.

3.5.1. ^{99m}Tc-BMBP complex preparation

Radiolabeling of compound **VI (BMBP)** using technetium-99 m as a radiotracer was done to prepare **^{99m}Tc-BMBP** complex. The highest radiochemical yield of **^{99m}Tc-BMBP** was 92.6 ± 2%. Such maximum yield was obtained using 1 mg of compound **BMBP** and 40 mg sodium dithionite. Radiolabeling reaction was done for 15 min reaction time at pH 6 at ambient temperature (27 ± 3 °C), Fig. 5**(A–D)**. The radiochemical purity was further confirmed by HPLC analysis, where the retention time of free $^{99m}TcO_4^-$ and **^{99m}Tc-BMBP** was 5 and 3.1 min, respectively as shown in the chromatogram **(**Fig. 6**)**. The *in-vitro* stability of **^{99m}Tc-BMBP** was up to 10 h.

Table 2
In-vivo biodistribution profile of ^{99m}Tc-BMBP complex in solid tumor bearing male Swiss albino mice (right thigh muscle) at different time intervals post-injection. (% ID/organ ± S.D, n = 5).

Organs	0.5 h	1 h	2 h	3 h	4 h
Blood	52.2	32.55	27.4	20.65	15.34
Kidneys	4.25	4.53	5.11	5.701	7.02
Liver	15.08	25.96	29.11	31.23	33.1
Spleen	0.82	1.35	1.75	2.08	1.33
Intestine	7.95	11.92	14.7	16.52	25.01
Stomach	1.91	3.84	4.92	5.88	4.25
Lungs	1.25	2.33	2.54	2.26	1.53
Heart	1.27	0.65	0.57	0.53	0.35
Bone	3.17	9.02	3.5	3.92	2.45
Normal left Muscle	10.52	12.17	9.42	9.71	9.05
Tumor right Muscle	21.8	26.54	27.25	29.7	39.82
T/NT	2.0722	2.1808	2.893	3.059	4.4

3.6. Pharmacokinetic study of ^{99m}Tc-BMBP complex

^{99m}Tc-BMBP biodistribution pattern is shown in Table 2. The complex uptake in solid tumor bearing muscle was higher than normal muscle at all time intervals. In addition, the values of target to non-target ratios (T/NT) were higher than 2 at most time intervals and reached a maximum value of 4.4 at 4 hr post injection. Liver and intestine high radioactivity levels indicate that hepatobiliary pathway is the main excretion route of ^{99m}Tc-BMBP. Low radioactivity levels of stomach indicate the good *in-vivo* stability of **^{99m}Tc-BMBP** [41–43].

3.7. Gamma scintigraphy of ^{99m}Tc-BMBP complex

Scintigraphic images of ^{99m}Tc-BMBP showed higher accumulation of radioactivity in right thigh compared to left thigh muscle at the first hour **(**Fig. 7**)**. Such higher accumulation increased with time and reached its maximum at 4 h due to radioactivity washout from the non-target organs. Consequently, scintigraphic imaging results matched with biodistribution results reflecting the high affinity of the compound **BMBP** to the tumor site [44,45].

4. Conclusion

Five substituted phenyl (azanediyl) bis (methylene phosphonic acid) derivatives; II, III, V, VI, VII were selected for synthesis as a result of computational screening of a number of amino phosphonic acid derivatives targeting HFPPS. These compounds showed high docking score of −23.65, −24.40–25.74–26.75, and −25.50 kcal/mol respectively. The computed affinity of **compound VI (BMBP)** was the top ranked 51.11 among all compounds. Molecular dynamic simulations of VI during 30 ns reached the equilibrium at 1.4 Å after 10 ns period. The tested compounds achieved inhibitory activity against HFPPS with IC_{50} of 39.9 μg/ml, 42.6 μg/ml, 63.1 μg/ml, 78.6 μg/ml and 79.3 μg/ml for VI, V, VII, II, and III respectively.

^{99m}Tc-BMBP complex was prepared by radiolabeling of compound VI using technetium-99 m as a radiotracer. The highest radiochemical yield of **^{99m}Tc-BMBP** was 92.6 ± 2%. The *in-vitro* stability of **^{99m}Tc-BMBP** was up to 10 h. The scintigraphic imaging results and biodistribution results confirmed the high affinity of the compound **BMBP** to the tumor site. Consequently, the tested substituted phenyl (azanediyl) bis (methylene phosphonic acid) scaffold was a successful inhibitor of HFPPS with stable radiolabeling properties that enabled it to be a selective scintigraphic imaging probe with anticancer activity.

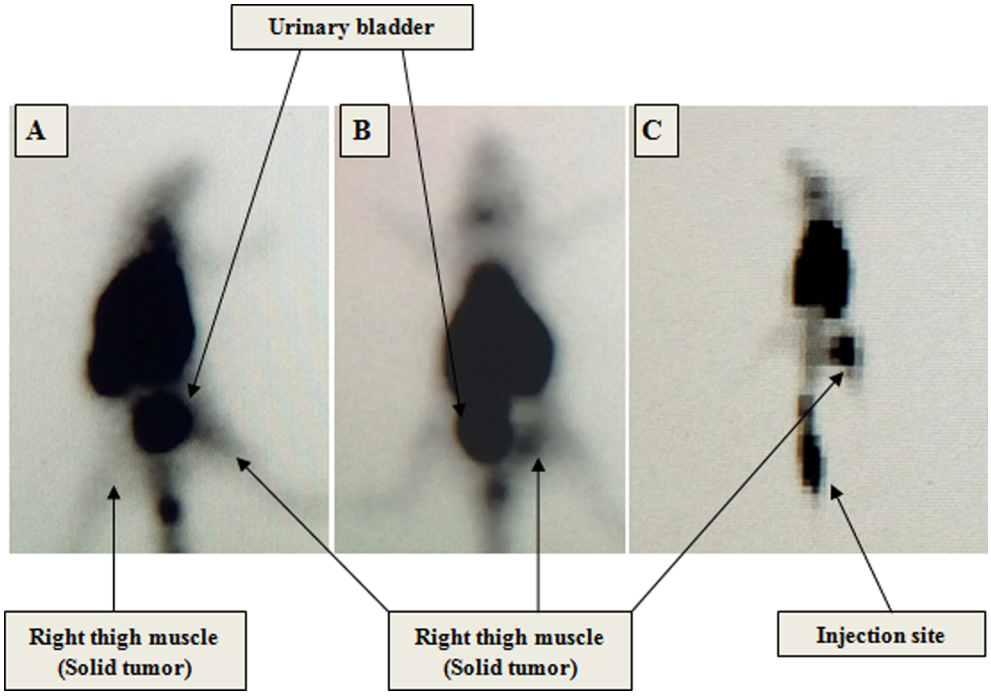

Fig. 7. Scintigraphic images of ^{99m}Tc-BMBP in mice at 1 hr (A), 2 hr (B) and 4 hr (C) post injection.

Ethical approval

Authors reported that all applicable international, national and institutional guidelines for the care and use of animals were followed.

Declaration of Competing Interest

Authors declared that they have no conflict of interest.

References

[1] Y. Tang, et al., A radiopharmaceutical [89Zr] Zr-DFO-nimotuzumab for immunoPET with epidermal growth factor receptor expression in vivo, Nucl. Med. Biol. 70 (2019) 23–31.
[2] T. Sakr, et al., In silico-based repositioning of phosphinothricin as a novel technetium-99m imaging probe with potential anti-cancer activity, Molecules 23 (2) (2018) 496.
[3] B. Pagano, S. Baldari, Radiopharmaceuticals for bone metastases, Clinical Applications of Nuclear Medicine Targeted Therapy, Springer, 2018, pp. 345–364.
[4] S. Rotman, et al., Drug delivery systems functionalized with bone mineral seeking agents for bone targeted therapeutics, J. Control. Release 269 (2018) 88–99.
[5] T.-J. Lin, Predicting binding affinities of nitrogen-containing bisphosphonates on hydroxyapatite surface by molecular dynamics, Chem. Phys. Lett. 716 (2019) 83–92.
[6] G.B. Saha, Nuclear pharmacy, Fundamentals of Nuclear Pharmacy, Springer, 2018, pp. 185–202.
[7] M. Motaleb, T. Sakr, Synthesis and preclinical pharmacological evaluation of 99mTc-TEDP as a novel bone imaging agent, J. Labelled Compd. Radiopharm. 54 (9) (2011) 597–601.
[8] S. Chakraborty, et al., Syntheses and evaluation of 68Ga-and 153Sm-labeled DOTA-conjugated bisphosphonate ligand for potential use in detection of skeletal metastases and management of pain arising from skeletal metastases, Chem. Biol. Drug Des. 92 (3) (2018) 1618–1626.
[9] V.D. Romanenko, Advances in the synthesis of functional α-organyl gem-bisphosphonates for biomedical applications, Adv. Organic Synthesis: Volume 12 12 (2018) 200.
[10] A. Grey, I.R. Reid, Differences between the bisphosphonates for the prevention and treatment of osteoporosis, Ther. Clin. Risk Manage. 2 (1) (2006) 77.
[11] B.L. Furman, Bisphosphonates. xPharm: The Comprehensive Pharmacology Reference, 2007; [1–3].
[12] M. Bermo, et al., Review of extraskeletal activity on Tc-99m methylene diphosphonate bone scintigraphy and value of cross-sectional and SPECT-CT imaging correlation, Curr. Probl. Diagn. Radiol. 47 (5) (2018) 324–332.
[13] M. Mitterhauser, S. Toegel, An in vitro model for the comparative evaluation of bone seeking pharmaceuticals, ALTEX-Alternat. Animal Experiment. 25 (1) (2008) 51–55.
[14] H. Liu, et al., Novel injectable calcium phosphate/chitosan composites for bone substitute materials, Acta Biomater. 2 (5) (2006) 557–565.
[15] N. Alves, et al., Designing biomaterials based on biomineralization of bone, J. Mater. Chem. 20 (15) (2010) 2911–2921.
[16] Q.Z. Liu, et al., 3D-QSAR, molecular docking, and ONIOM studies on the structure–activity relationships and action mechanism of nitrogen-containing bisphosphonates, Chem. Biol. Drug Des. 91 (3) (2018) 735–746.
[17] D.D. Waller, J. Park, Y.S. Tsantrizos, Inhibition of farnesyl pyrophosphate (FPP) and/or geranylgeranyl pyrophosphate (GGPP) biosynthesis and its implication in the treatment of cancers, Crit. Rev. Biochem. Mol. Biol. 54 (1) (2019) 41–60.
[18] S.A. Holstein, R.J. Hohl, Inhibition of farnesyl and geranylgeranyl diphosphate synthases, Enzymes 30 (2011) 301–319.
[19] A. Hellal, S. Chafaa, N. Chafai, Synthesis, characterization and computational studies of three α-amino-phosphonic acids derivatives from Meta, Ortho and Para aminophenol, J. Mol. Struct. 1103 (2016) 110–124.
[20] T. Mosmann, Rapid colorimetric assay for cellular growth and survival: application to proliferation and cytotoxicity assays, J. Immunol. Methods 65 (1–2) (1983) 55–63.
[21] S.M. Gomha, et al., Synthesis and anticancer activities of thiazoles, 1, 3-thiazines, and thiazolidine using chitosan-grafted-poly (vinylpyridine) as basic catalyst, Heterocycles 91 (6) (2015) 1227–1243.
[22] N. Geskovski, et al., Comparative biodistribution studies of technetium-99 m radiolabeled amphiphilic nanoparticles using three different reducing agents during the labeling procedure, J. Labelled Compd. Radiopharm. 56 (14) (2013) 689–695.
[23] R.M. Abd-Elal, et al., Trans-nasal zolmitriptan novasomes: in-vitro preparation, optimization and in-vivo evaluation of brain targeting efficiency, Drug Delivery 23 (9) (2016) 3374–3386.
[24] H.M. Rashed, R.N. Shamma, H.A. El-Sabagh, Preparation of 99mTc-levetiracetam intranasal microemulsion as the first radiotracer for SPECT imaging of the Synaptic Vesicle Protein SV2A, Eur. J. Pharm. Sci. 121 (2018) 29–33.
[25] T. Nasr, et al., Novel hydrazide-hydrazone and amide substituted coumarin derivatives: synthesis, cytotoxicity screening, microarray, radiolabeling and in vivo pharmacokinetic studies, Eur. J. Med. Chem. 151 (2018) 723–739.
[26] H.M. Rashed, R.N. Shamma, E.B. Basalious, Contribution of both olfactory and systemic pathways for brain targeting of nimodipine-loaded lipo-pluronics micelles: in vitro characterization and in vivo biodistribution study after intranasal and intravenous delivery, Drug Delivery 24 (1) (2017) 181–187.
[27] H. Rashed, I. Ibrahim, M. Motaleb, 99m Tc-hexoprenaline and 131 I-dapoxetine: preparation, in silico modeling and biological evaluation as promising lung scintigraphy radiopharmaceuticals, J. Radioanal. Nucl. Chem. 314 (2) (2017) 1297–1307.
[28] M. Sanad, et al., In silico study and biological evaluation of 99mTc-tricabonyl oxiracetam as a selective imaging probe for AMPA receptors, J. Radioanal. Nucl. Chem. 314 (3) (2017) 1505–1515.
[29] T.M. Sakr, et al., Preparation and biological profile of 99m Tc-lidocaine as a cardioselective imaging agent using 99m Tc eluted from 99 Mo/99m Tc generator based on Al–Mo gel, J. Radioanal. Nucl. Chem. 314 (3) (2017) 2091–2098.
[30] T.H. Bokhari, et al., Preparation, biodistribution and scintigraphic evaluation of 99m Tc-lincomycin, Pak. J. Pharm. Sci 28 (6) (2015) 1965–1970.
[31] M.U. Akbar, et al., A review on evaluation of technetium-99m labeled

radiopharmaceuticals, J. Radioanal. Nucl. Chem. 310 (2) (2016) 477–493.
[32] B. Essa, et al., 99m Tc-amitrole as a novel selective imaging probe for solid tumor: In silico and preclinical pharmacological study, Eur. J. Pharm. Sci. 76 (2015) 102–109.
[33] R.I. Al-Wabli, et al., Platelet-12 lipoxygenase targeting via a newly synthesized curcumin derivative radiolabeled with technetium-99m, Chem. Cent. J. 10 (1) (2016) 73.
[34] W.x. Wan, et al., [99mTc] polyamine analogs as potential tumor imaging agent, Drug Dev. Res. 69 (8) (2008) 520–525.
[35] T. Sakr, et al., Biodistribution of 99mTc-sunitinib as a potential radiotracer for tumor hypoxia imaging, J. Labelled Compd. Radiopharm. 56 (8) (2013) 392–395.
[36] T. Sakr, et al., Synthesis and biodistribution of 99m Tc-PyDA as a potential marker for tumor hypoxia imaging, Radiochemistry 56 (1) (2014) 76–80.
[37] N. Arulsudar, et al., Preparation, characterization, and biodistribution study of technetium-99m-labeled leuprolide acetate-loaded liposomes in ehrlich ascites tumor-bearing mice, AAPS PharmSci 6 (1) (2004) 45–56.
[38] S.A. Nour, et al., Intranasal brain-targeted clonazepam polymeric micelles for immediate control of status epilepticus: in vitro optimization, ex vivo determination of cytotoxicity, in vivo biodistribution and pharmacodynamics studies, Drug Delivery 23 (9) (2016) 3681–3695.
[39] D.L. Hawary, et al., Water-soluble derivatives of chitosan as a target delivery system of 99mTc to some organs in vivo for nuclear imaging and biodistribution, J. Radioanal. Nucl. Chem. 290 (3) (2011) 557–567.
[40] E.-M. Kim, et al., Hepatocyte-targeted nuclear imaging using 99mTc-galactosylated chitosan: conjugation, targeting, and biodistribution, J. Nucl. Med. 46 (1) (2005) 141–145.
[41] H. Rashed, F. Marzook, H. Farag, 99m Tc-zolmitriptan: radiolabeling, molecular modeling, biodistribution and gamma scintigraphy as a hopeful radiopharmaceutical for lung nuclear imaging, Radiol. Med. (Torino) 121 (12) (2016) 935–943.
[42] R.M. Harden, W. Alexander, I. Kennedy, Isotope uptake and scanning of stomach in man with 99mTc-pertechnetate, Lancet 289 (7503) (1967) 1305–1307.
[43] H. Rashed, I. Ibrahim, M. Motaleb, 99mTc-hexoprenaline and 131I-dapoxetine: preparation, in silico modeling and biological evaluation as promising lung scintigraphy radiopharmaceuticals, J. Radioanal. Nucl. Chem. (2017) 1–11.
[44] D.-W. Kim, et al., Synthesis and evaluation of Tc-99m-labeled RRL-containing peptide as a non-invasive tumor imaging agent in a mouse fibrosarcoma model, Ann. Nucl. Med. 29 (9) (2015) 779–785.
[45] D.W. Kim, et al., Synthesis and evaluation of novel Tc-99 m labeled NGR-containing hexapeptides as tumor imaging agents, J. Labelled Compd. Radiopharm. 58 (2) (2015) 30–35.